Yusheng Wang[1]
Department of Mechanical
and Aerospace Engineering,
University of California, Irvine,
4200 Engineering Gateway,
Irvine, CA 92697
e-mail: yushengw@uci.edu

Mohammad H. Asadian
Department of Mechanical
and Aerospace Engineering,
University of California, Irvine,
4200 Engineering Gateway,
Irvine, CA 92697
e-mail: asadianm@uci.edu

Andrei M. Shkel
Department of Mechanical
and Aerospace Engineering,
University of California, Irvine,
4200 Engineering Gateway,
Irvine, CA 92697
e-mail: andrei.shkel@uci.edu

Modeling the Effect of Imperfections in Glassblown Micro-Wineglass Fused Quartz Resonators

In this paper, we developed an analytical model, supported by experimental results, on the effect of imperfections in glassblown micro-wineglass fused quartz resonators. The analytical model predicting the frequency mismatch due to imperfections was derived based on a combination of the Rayleigh's energy method and the generalized collocation method. The analytically predicted frequency of the n = 2 wineglass mode shape was within 10% of the finite element modeling results and within 20% of the experimental results for thin shells, showing the fidelity of the predictive model. The postprocessing methods for improvement of the resonator surface quality were also studied. We concluded that the thermal reflow of fused quartz achieves the best result, followed in effectiveness by the RCA-1 surface treatment. All the analytical models developed in this paper are to guide the manufacturing methods to reduce the frequency and damping mismatch, and to increase the mechanical quality factor of the device.
[DOI: 10.1115/1.4036679]

1 Introduction

There are two modes of microelectromechanical systems (MEMS) coriolis vibratory gyroscope (CVG) operation: the rate mode, in which the gyroscope measures the angular rate of rotation, and the rate-integrating mode, or whole-angle mode, in which the gyroscope directly measures the angle of rotation. Advantages of the whole-angle mode gyroscope, such as fundamentally unlimited mechanical bandwidth of operation and linearity of response throughout the entire range of operation, are broadly recognized. The ability of the sensor to operate in the rate-integrating mode, however, is completely determined by axial symmetry of the mechanical structure and isotropy of the structural material. Some initial results toward isotropic designs have been presented in Refs. [1–3], indicating a potential of MEMS-fabricated devices for inertial guidance applications.

In addition to structural symmetry, the quality factor is another critical parameter, which is essential to enhance the performance of vibratory inertial MEMS devices [4]. A better in-run noise performance, such as bias stability and angle random walk (ARW), can be achieved with a higher quality factor of resonating structures. Many factors, such as viscous air damping, anchor losses, thermo-elastic dissipation, and surface-related losses, influence the overall quality factor of the resonators. Surface-related losses were reported to dominate the quality factor of the large-scale hemispherical resonator gyroscope (HRG), showing an inverse relationship between the quality factor and the surface-to-volume ratio [5]. Surface-related losses are believed to be associated with surface roughness, contaminations, absorbates, moisture, and oxidized layer on the surface, but the results are still not conclusive on the dominant factors. In this paper, we hypothesized that the surface roughness of glassblown fused quartz resonators is the dominant factor of the energy losses and we provide evidences in support of this hypothesis.

The accuracy of intended geometry of conventional two-dimensional (2D) MEMS fabrication is limited by lithography and etching imperfections. For example, a typical resolution of ultraviolet lithography is on the order of 0.1 micron and a typical aspect ratio of dry etching of material is 20:1. The whole-angle mode of operation, however, imposes strict requirements on structural and damping symmetry as well as the quality factor of devices, which cannot be readily achieved by conventional 2D MEMS fabrication due to its limitations in accuracy of lithography and etching-based manufacturing. While the conventional MEMS processes are improving, new design architectures and fabrication processes for high precision of manufacturing are emerging [6].

Macroscale HRG has demonstrated high structural symmetry and low energy losses, and this subsequently led to higher sensitivity and lower drift, as well as a superior survivability to environmental shocks and vibrations [7]. Advances in three-dimensional (3D) macroshell structures inspired the development of 3D microscale resonators for vibratory inertial MEMS devices, emphasizing the potential for batch manufacturing and reduced cost [6]. Generally, there are two main methods that have been recently explored for fabrication of microscale 3D resonators: (1) thin film deposition of materials in a predefined micromachined mold, lithographic patterning, and chemical release and (2) thermo-elastic "blowing" of the device layer and a subsequent mechanical release by mechanical lapping or chemical–mechanical polishing (CMP).

In the first approach, a hemispherical mold is first defined by wet etching or machining. Then, a sacrificial layer is deposited in the mold. It is followed by material deposition on the sacrificial layer to define the resonator. Finally, the sacrificial layer is chemically removed to release the resonator. The benefits of this process include a near-conventional MEMS fabrication process and its compatibility with a wide range of materials, such as polysilicon, polydiamond, and silicon dioxide. For example, ultralow

expansion (ULE) glass hemispherical shell with $1.2\,\mu m$ thickness was demonstrated in Ref. [8] with the reported thickness variation better than 120 ppm and dimensional deviations of less than $0.125\,\mu m$. In those first demonstrations, only one resonant peak was observed and it was explained by a high structural isotropy. A polysilicon hemispherical resonator formed by deposition in the mold has also been demonstrated, with the resonant frequency of 6.7 kHz and the quality factor of 8500 [9]. No metrology on thickness variation and deviation in dimensions were reported. The quality factor as high as 143,000 at 15.6 kHz was measured on polycrystalline diamond hemispherical resonator with 2 Hz as-fabricated frequency mismatch [10]. Surface quality and structural symmetry were usually low for devices fabricated from mold-associated processes because the roughness and the asymmetry of the mold were likely to be transferred to the device. The polycrystalline structure is also likely to increase an intrinsic dissipation of the devices due to the grain structure of the material. To date, the mold-associated processes were limited in symmetry and quality factor, and alternative fabrication processes for high-performance 3D resonators were investigated.

A highly promising technique is a thermo-elastic blowing of materials. Microglassblowing on a wafer level was first introduced in Ref. [11]. In this initial study, Pyrex spherical shells were fabricated demonstrating the surface roughness of less than 1 nm. Fabrication of Pyrex or fused quartz 3D microresonators without utilization of molds was first proposed in Ref. [12] by microglassblowing technique. This approach took the advantage of pressure difference and surface tension driven plastic deformation of the glass wafer to form 3D structures, demonstrated to be compatible with wafer-level fabrication. A microblowtorch molding process, which is a variation of the glassblowing technique, was utilized to fabricate "birdbath" fused quartz shell resonators, demonstrating 1.2×10^6 quality factor, 0.5 nm surface roughness, and 6.7 Hz frequency split [13]. Thermoplastic forming of bulk metallic glass (BMG) was first demonstrated with utilization of mold in Ref. [14] and an improved fabrication process was demonstrated with $Pt_{57.5}Cu_{14.7}Ni_{5.3}P_{22.5}$ bulk metallic glass (Pt-BMG), resulting in hemispherical shells with the surface roughness less than 0.3 nm [15]. The quality factor of the BMG devices demonstrated in Ref. [15] was on the level of 6200 and the frequency mismatch on the level of 4.9 Hz. In these two processes, although molds were needed to define the geometry of the resonators, the surface of the resonator did not make a contact with the mold, and therefore a high surface quality was achieved. Currently, the blowtorch and the thermoplastic forming of BMG processes are not completely compatible with MEMS batch fabrication due to the methods of heating and applying the pressure difference individually to each shell. The use of an array of torches has been considered [16], for scaling the technique to batch fabrication.

In contrast to the technique of material deposition in a mold (method 1 described above), the structural symmetry of the "blown" shells (method 2 described above) was leveraged by the symmetric nature of glassblowing. To further reduce the thermo-elastic damping (TED), materials with low coefficient of thermal expansion (CTE), such as fused quartz, were considered [17]. Sub-Hz frequency mismatch, as low as 0.16 Hz, on Pyrex resonators [18] and the quality factor of over 1.1×10^6 on fused quartz resonators have been reported [19]. Despite the potential advantages of 3D microglassblowing, the fabrication imperfections were still inevitable, with a typical quality factor on the order of 100,000 and the frequency mismatch on the order of 10 Hz. The observed effects were not merely due to glassblowing process, but due to the additional mechanical lapping and chemical processing steps accompanying the process. For example, the fused quartz wafers would go through many wet etching steps before the final glassblowing step. These steps include hydrogen fluoride (HF) etching of the wafer, polysilicon hard mask removal in potassium hydroxide (KOH), and standard RCA-1 wafer cleaning [18]. All these steps will influence the surface roughness of the wafers and their effects may not be eliminated completely by glassblowing
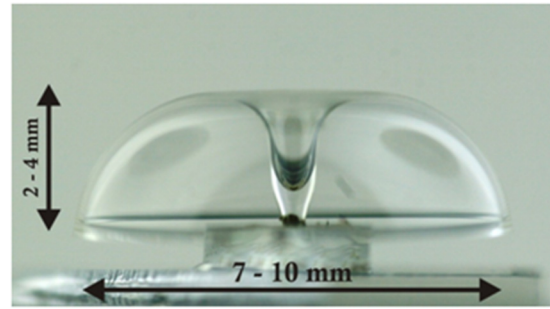
Fig. 1   Hemitoroidal shell fabricated using high-temperature microglassblowing process of fused quartz

[20]. Additionally, glassblown 3D microshells were released by a multistep mechanical lapping process to optimize the quality of the lapped surface. The process may introduce structural imperfections to the sensing element if the lapping plane is not completely aligned [21]. This paper presents an analytical model to predict the effects of fabrication imperfections due to asymmetric lapping as one of the sources of imperfections.

In previous studies, 10:1 HF/HCl etching was reported to create a smoother surface on Pyrex and soda-lime-glass than the HF etching [22]. Buffered oxide etching (BOE) was reported to improve the surface of fused quartz devices [13]. However, no systematic studies and comparative analyses of fused quartz etching processes have been reported in the literature. In this work, we investigate the effects of thermal and chemical postprocessing on the surface quality of fused quartz wafers and propose a method to further smoothen the surface of resonators based on the obtained results.

An analytical frequency model of hemitoroidal shell is developed in the paper. The model is used to understand the behavior of the system and the effects of imperfections in a more direct way than the finite element model would allow. The operational frequency and frequency mismatch estimations of macromachined hemispherical shells have been thoroughly studied in Ref. [23]. Microfabricated shells, however, take shapes closer to hemitorus than hemisphere (Fig. 1). Directly applying the analytical models developed for hemispherical shells to hemitoroidal shells may lead to large errors, with modeling errors of over 50% for shells with comparable thickness and outer radius [21]. No analytical models predicting the frequency of hemitoroidal shells have been previously developed. To fulfill the gap, this paper develops models predicting the frequency response of hemitoroidal shells due to imperfections induced by the release process.

In the following sections, we first present the analytical model of hemitoroidal shell for predicting the resonant frequency, and then the experimental verification of the results is discussed in Sec. 2. This is followed by extension of the model for the frequency mismatch prediction for microscale glassblown structures, Sec. 3. In Sec. 4, the effects of different thermal and chemical postprocesses are characterized and analyzed both on flat and curved surfaces. The thermal reflow of fused quartz achieved the best result, followed in effectiveness by the RCA-1 surface treatment. In Sec. 5, the fused quartz wineglass resonators with different surface quality are characterized, demonstrating the direct correlation between surface roughness and the quality factor. The paper concludes with a discussion of results in Sec. 6.

2   Frequency Model

In this section, we introduce an analytical model of hemitoroidal shell based on the inextensional wineglass mode shape assumption. The natural frequency of a perfectly symmetric shell was derived by applying the Rayleigh's energy method and verified experimentally.

2.1 Derivation of Mode Shapes. Figure 2 shows a thin hemitoroidal shell with thickness h and radius R. In spherical coordinates, the shape of the shell can be expressed as $r = 2R \sin \theta$, where r is the radial distance and θ is the polar angle. Since the shell is axisymmetric, r is independent of φ, and the latter is defined as the azimuth angle. Movement of the shell structure is completely described by the movement of its middle surface. We assume the local displacement components of the middle surface are defined by δr, $\delta \theta$, and $\delta \varphi$, where δr is the linear displacement along r, while $\delta \theta$ and $\delta \varphi$ are the angular displacements along θ and φ, respectively. In the wineglass mode, the displacement components of two matched modes are expressed as

$$
\begin{array}{ll}
\delta r = U(\theta) \sin n\varphi \cos \omega t & \delta r = U(\theta) \cos n\varphi \cos \omega t \\
\delta \theta = V(\theta) \sin n\varphi \cos \omega t \quad \text{and} & \delta \theta = V(\theta) \cos n\varphi \cos \omega t \\
\delta \varphi = W(\theta) \cos n\varphi \cos \omega t & \delta \varphi = W(\theta) \sin n\varphi \cos \omega t
\end{array}
$$

$$(1)$$

where n is called the mode number, ω is the angular frequency of the mode, and U, V, and W are mode shape functions of variable θ [24], and they are to be determined later in this section. The terms in Eq. (1) containing φ define the orientation of the mode shape and the terms containing ω define the frequency. Note that orientations of the mode shapes with respect to the azimuth angle are separated by $\pi/2n$. For $n = 2$ wineglass mode, for example, the orientations of mode shapes are separated by 45 deg.

Inextensional assumption is applied to calculate the mode shape functions. It assumes that the strain of the middle surface of the shell remains zero during the deformation. This assumption holds if thickness of the shell is much smaller than the other dimensions [24]. In the case of glassblown structures, the thickness of the shell is on the order of $100 \, \mu m$, while the outer radius is on the order of $10 \, mm$ and the height is about $3 \, mm$ (Fig. 1). Hence, due to the ratio of dimensions (100:1 and 30:1), the inextensional assumption is justifiable to apply for the structures of interest.

Let us consider an arbitrary line element with length ds on the middle surface of the shell at position (r, θ, φ) and its length components dr, $d\theta$, and $d\varphi$. After deformation of the shell, the position of the element becomes $(r + \delta r, \theta + \delta \theta, \varphi + \delta \varphi)$ and its length becomes $ds + d\delta s$. In the spherical coordinate system, the length of the line element can be expressed as

$$
(ds + d\delta s)^2 = (dr + d\delta r)^2 + (r + \delta r)^2 \sin^2(\theta + \delta \theta)(d\varphi + d\delta \varphi)^2
$$
$$
+ (r + \delta r)^2 (d\theta + d\delta \theta)^2 \qquad (2)
$$

We expand the differential elements in displacement and geometry with respect to coordinates θ and φ as follows:

$$
d\delta r = \frac{\partial \delta r}{\partial \theta} d\theta + \frac{\partial \delta r}{\partial \varphi} d\varphi
$$

$$
d\delta \theta = \frac{\partial \delta \theta}{\partial \theta} d\theta + \frac{\partial \delta \theta}{\partial \varphi} d\varphi
$$

$$
d\delta \varphi = \frac{\partial \delta \varphi}{\partial \theta} d\theta + \frac{\partial \delta \varphi}{\partial \varphi} d\varphi
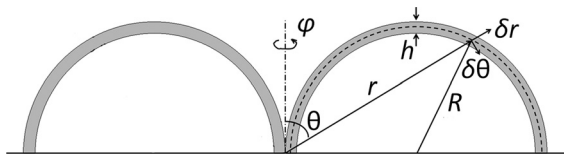$$

$$
dr = \frac{dr}{d\theta} d\theta
$$

Fig. 2 Coordinate system, middle surface (dashed line), and parameters of hemitoroidal shell

The radial distance of hemitorus r is only dependent on the polar angle θ and not related to the azimuth angle φ. Therefore, there is no $d\varphi$ term in the expansion of dr.

When we consider only the first-order terms in Eq. (2), the resulting equation for the deformation of the line element takes the form

$$
\frac{d\delta s}{ds} = \left(\frac{dr}{d\theta} \frac{\partial \delta r}{\partial \theta} + r^2 \frac{\partial \delta \theta}{\partial \theta} + r \delta r \right) \frac{d\theta^2}{ds^2}
$$
$$
+ \left(r \delta r \sin^2 \theta + r^2 \sin \theta \cos \theta \delta \theta + r^2 \frac{\partial \delta \varphi}{\partial \varphi} \sin^2 \theta \right) \frac{d\varphi^2}{ds^2}
$$
$$
+ \left(\frac{dr}{d\theta} \frac{\partial \delta r}{\partial \varphi} + r^2 \frac{\partial \delta \theta}{\partial \varphi} + r^2 \frac{\partial \delta \varphi}{\partial \theta} \sin^2 \theta \right) \frac{d\theta d\varphi}{ds^2} \qquad (3)
$$

According to the inextensional assumption, the length of the line element should not change after deformation no matter what values dr, $d\theta$, and $d\varphi$ would take, implying that the coefficients of all terms on the right-hand side of Eq. (3) are zero. Substituting Eq. (1) in Eq. (3) and canceling the two variables δr and $\delta \theta$ would cancel the common orientation term (sinusoidal term with respect to φ) and the frequency term (sinusoidal term with respect to t). The resulting fundamental equation of the mode shape of the hemitoroidal shell becomes

$$
\left(\cos^2 \theta - \sin^2 \theta \right) \frac{d^2 r_\varphi}{d\theta^2} + 4 \sin \theta \cos \theta \frac{dr_\varphi}{d\theta} + \frac{2n^2 - 1}{\sin^2 \theta} r_\varphi = 0 \quad (4)
$$

where $r_\varphi = r \, W(\theta) \sin \theta$ represents the linear displacement along the azimuth angle. We are solving Eq. (4) for r_φ instead of $W(\theta)$ to avoid the coefficient of the second-order term from being zero when $\theta = 0$. Note that the mode number n is included in Eq. (4), indicating that the equation allows to calculate the mode shapes of any order.

Equation (4) is a linear second-order ordinary differential equation with varying coefficients. A clamped boundary condition was assumed at $\theta = 0$, corresponding to the attachment of the stem of the device to a substrate. The collocation method was applied to solve the equation numerically [25]. Hermite polynomials of order three were used to approximate the solution. The solution with $n = 2$ is shown by the solid line in Fig. 3. The dashed line in Fig. 3 is the normalized result from finite element analysis (FEA); COMSOL MULTIPHYSICS package was used for the FEA modeling. Convergence of the analysis was achieved with meshing elements on the order of 25,000. The largest error was about 1% of the maximum displacement, where θ was about 0.5 rad. The small error indicates the fidelity of the developed analytical model. Note that the amplitude of motion is close to zero when $\theta < \pi/4$,
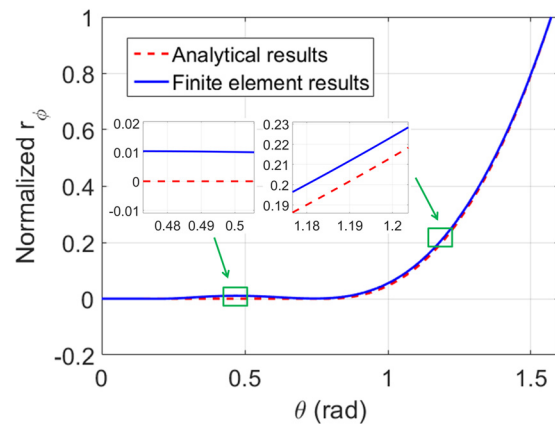

Fig. 3 Comparison of $n = 2$ mode shapes from analytical model and finite element model. Displacements in φ direction are normalized.

corresponding to the inner part of the device, and the vibratory energy is mostly limited in the outer part of the device. It implies that geometric deviation of the inner part of the real device from the model will only induce a small disturbance of the resonant frequency of the device, which expands the range where the model can be applied.

2.2 Calculation of Resonant Frequency. Resonant frequency of the shell was derived by the Rayleigh's energy method [23]. First, the kinetic energy K_0 and the strain energy U_0 of the shell were calculated based on the mode shape with an arbitrary amplitude of motion A

$$K_0 = \frac{1}{2}\rho \iiint_\Omega \left(\dot{\delta} r^2 + r^2 \dot{\delta}\theta^2 + r^2 \sin^2\theta \dot{\delta}\varphi^2\right)dV \qquad (5)$$

$$U_0 = \frac{1}{2}\iiint_\Omega \left(\sigma_{11}\varepsilon_{11} + \sigma_{22}\varepsilon_{22} + \sigma_{12}\varepsilon_{12}\right)dV \qquad (6)$$

where Ω is the integration region, which is the shape of the shell. Directions 1 and 2 in Eq. (6) are the two principal axes of the middle surface, corresponding to θ and φ directions. For shells with thicknesses much smaller than the other dimensions, the strain related to the third direction (normal direction) is zero [26]. This is the reason why there are only three terms instead of six in parenthesis of Eq. (6). Then, the Lagrangian was expressed as $L = U_{0max} - K_{0max}$, where U_{0max} and K_{0max} are correspondently the maximum of the kinetic energy and the strain energy with respect to time. Finally, solving the Rayleigh's equation $\partial L/\partial A = 0$ gave us the angular frequency of the shell.

As shown in Fig. 4, the analytical model matches well with the finite element model for the $n = 2$ mode. The error is within 10% for the shell with thickness less than $300\,\mu m$. Since inextensional assumption can only be applied to thin shells, larger errors for thicker shells are expected. In such cases, the complexity of the model should be increased by eliminating the inextensional assumption and using the full tensor of deformation.

2.3 Experimental Verification. Frequencies of microshells with outer diameter of $7\,mm$ and thicknesses of $70\,\mu m$, $150\,\mu m$, and $250\,\mu m$ were tested to verify the analytical model. The shells were actuated along the stem by a piezoelectric element attached to the shell by Field's metal and characterized optically by laser Doppler vibrometer (LDV) in a vacuum chamber under pressure on the order of $20\,\mu Torr$, so that the viscous air damping is completely eliminated [19]. The experimental setup is shown in Fig. 5. The results are presented in Fig. 4, showing the maximum errors of about 20%, when the shell thickness is less than $150\,\mu m$. The errors are possibly due to nonuniformity of the thickness and

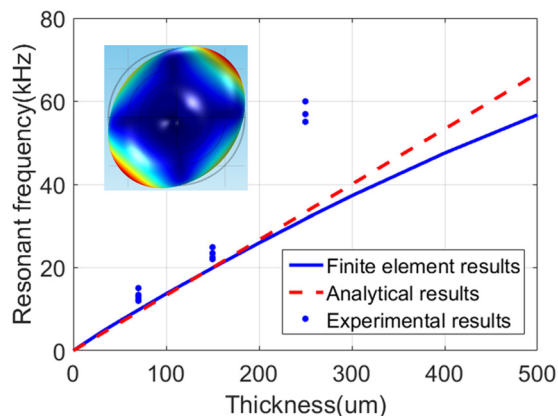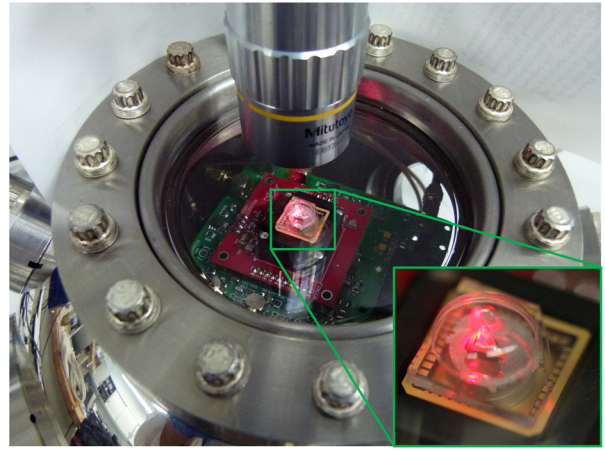**Fig. 5 Experimental setup to measure the resonant frequency of the device**

over-release of the devices. For thicker devices, the errors are relatively larger because the shells are not fully developed during glassblowing and consequently the shape deviates from the hemitorus.

3 Frequency Mismatch Model

The shell release is a step in the fabrication process where the substrate of glassblown structure is physically removed [18]. The mechanical lapping is the method used in our study for release. An additional frequency mismatch may be introduced if the lapping plane is not strictly perpendicular to the stem of the shell, Fig. 6. This phenomenon is studied both analytically and experimentally.

3.1 Analytical Results. The mode shape of a resonator can be considered unaffected by a small structural disturbance [23]. Therefore, in this study, we only have to change the integration region in Eqs. (5) and (6) from axisymmetric region to the actual shape of the shell, without recalculating the mode shape itself. For a perfectly symmetric shell, the integration results for both modes are the same and therefore the frequency mismatch is zero. For shells with lapping imperfections, the integration results will be different due to the asymmetric integration region, and therefore, the frequencies of the two mode shapes will be different. The relation between the angular lapping error (β) and the ratio between the frequency mismatch and frequency is shown in Fig. 6.

3.2 Experimental Results. Special lapping fixtures were designed and fabricated by 3D printing to release shells with a
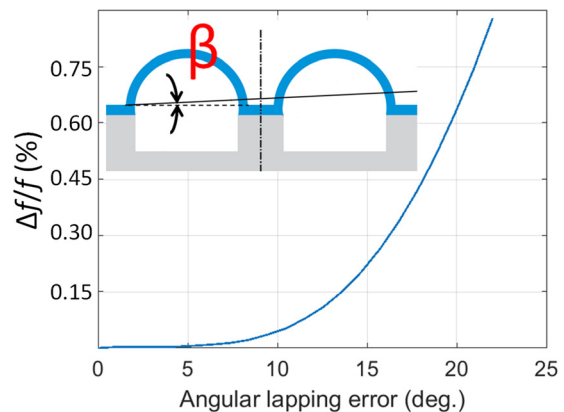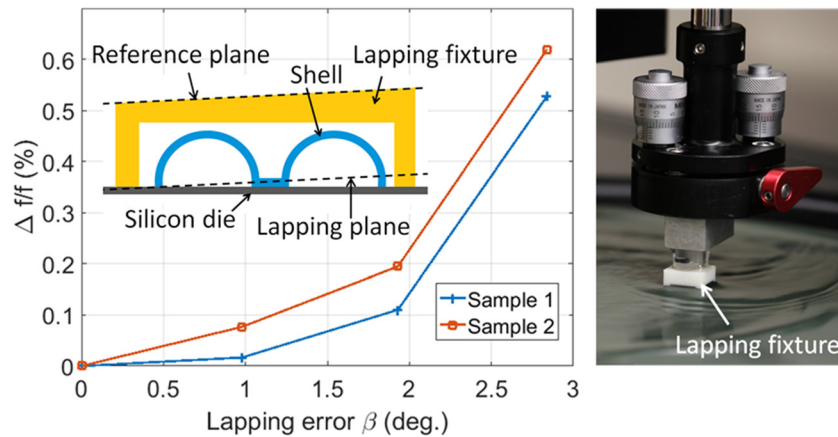

Fig. 4 Relation between resonant frequency of $n = 2$ mode and the thickness of the shell

Fig. 6 Schematic of lapping error and the analytical result

Fig. 7 Schematic of the attachment of device to lapping fixture and a picture of a device being asymmetrically lapped is presented. Experimental result of the effects of lapping imperfections is also shown.

specific lapping angle, Fig. 7. The lapping fixtures were designed to create the tilt angle of 1 deg. This allows the lapping angular error to increase by 1 deg after each subsequent lapping cycle. The microfabricated shells were first attached to a silicon die by Crystalbond 509-3. The silicon die was used as a reference plane coinciding with the edge of the shell. Then, the silicon die together with the shell was attached to the lapping fixture. Figure 7 shows a device being asymmetrically lapped and the silicon die has been lapped away. The shell was cleaned and characterized by LDV after each asymmetric lapping.

The results shown in Fig. 7 illustrate the predicted effect. The model confirms the trend of changes. The experimental change of frequency mismatch increases faster than the model predicts. One possible reason might be the fact that thickness of the rim of the shell is much larger than in other regions of the shell. Therefore, the real effects of asymmetric lapping on the frequency mismatch might be larger than predicted. The other reason might be the large initial frequency mismatches of the two shells tested, which were 105 Hz and 202 Hz, respectively, corresponding to about 1.5% and 3% of the resonant frequency. The large frequency mismatch causes the shape of the shell to deviate from the model, and consequently the error might be significant between the model and the experiment.

4 Postprocessing for Surface Quality

To increase the quality factor of the micro-wineglass fused quartz resonators, different thermal and chemical postprocessing techniques were tested to optimize the surface quality of the device and the results are discussed in this section. In our study, the effects of thermal and chemical postprocesses were initially tested on blank fused quartz wafers. Then, the effects of thermal reflow were tested on curved 3D fused quartz structures to show that the conclusions derived from blank samples are applicable to curved surfaces.

4.1 Experimental Procedure on Flat Samples. In our initial experiments, fused quartz wafers were first diced into 5 mm × 5 mm samples before different postprocessing methods were conducted on the samples. The tested postprocessing methods included thermal reflow, KOH etching, buffered oxide etching (BOE), 10:1 hydrogen fluoride and hydrogen chloride solution (HF/HCl) etching, and RCA-1 surface treatment. Atomic force microscope (AFM) from pacific nanotechnology (Nano-R) was used to measure the surface roughness of samples and the scan area was 10 μm × 10 μm for blank fused quartz samples. All samples were measured at three different points to guarantee the reliability of the measurement. The samples were cleaned by a standard solvent cleaning procedure (acetone, isopropyl alcohol, methanol) before each scan. The AFM was run in a close contact mode, using a 10 nm radius probe tip (Agilent U3120A).

4.2 Results and Discussion

4.2.1 Chemical Postprocessing. Fused quartz wafers went through a number of chemical processing steps before they were fabricated into wineglass resonators. All these processing steps have an influence on the surface quality of samples. Typical processes included 48% HF etching, 45% KOH hard mask removal, and RCA-1 cleaning. Some processes also include 10:1 HF/HCl etching and BOE. The effects of all these treatments on the surface quality of fused quartz were investigated and are reported in this section. Each treatment was applied to samples for the time duration that is typical for the fabrication process of wineglass resonator. The results are summarized in Table 1.

Table 1 shows that both KOH etching and BOE deteriorate the surface of fused quartz, and HF etching created a lower surface roughness than 10:1 HF/HCl solution, while RCA-1 surface treatment improved the surface quality of fused quartz samples by reducing the averaged surface roughness from 6.3 nm Sa to 4.7 nm Sa. To uncover the active components of RCA-1 solution and to understand mechanisms of the effect, three fused quartz samples with the same surface quality were placed into RCA-1 solution (volume ratio of 1:1:5 for 27% NH_4OH, 30% H_2O_2, and deionized (DI) water), H_2O_2 solution (0:1:6), and NH_4OH solution (1:0:6), respectively. The reaction temperature was controlled at 80 °C and the reaction time was 20 min for all three samples. The results are shown in Table 2.

Table 1 Effects of different chemical treatments on surface roughness

Comparison	Sample status	Surface roughness Sa[a] (nm)			
		Point 1	Point 2	Point 3	Averaged
1	Original	25.7	25.2	22.6	24.5
	10 min KOH	50.5	47.7	47.8	48.7
2	Original	1.2	1.1	1.2	1.2
	30 s BOE	5.4	5.2	5.5	5.4
	5 h HF	1.7	1.3	1.0	1.3
	5 h 10:1 HF/HCl	10.7	12.0	9.4	10.7
3	Original	7.5	5.6	5.8	6.3
	20 min RCA-1	4.3	5.1	4.8	4.7

[a]Sa denotes the arithmetic average of a height function of a surface.

Table 2 Effects of RCA-1 and its components

| | Surface roughness Sa (nm) | | | |
Sample status	Point 1	Point 2	Point 3	Averaged
Original	7.5	5.6	5.8	6.3
RCA-1	4.3	5.1	4.8	4.7
H$_2$O$_2$	7.5	6.1	6.2	6.6
NH$_4$OH	6.2	5.5	5.7	5.8

The results show that H$_2$O$_2$ or NH$_4$OH alone did not greatly change the surface quality; however, their combination reduced the averaged surface roughness from 6.3 nm Sa to 4.7 nm Sa. According to Ref. [27], the SiO$_2$ etching rate is on the order of 0.1 nm/min and it increases with increasing NH$_4$OH/H$_2$O$_2$ ratio and with increasing the temperature. This result suggests that the surface roughness of a sample may become worse if a higher etching rate is applied with certain etchants.

4.2.2 Thermal Postprocessing. Fused quartz is an amorphous material that does not have a precisely defined melting temperature. As the temperature increases, the material becomes soft and its viscosity decreases. If the temperature of treatment is high enough, the surface tension of fused quartz can overcome viscosity and therefore can minimize the surface area, like in a liquid. Using the reflow phenomenon, the surface roughness can be improved.

Reflow temperature is one of the critical parameters during the reflow of 3D devices. On the one hand, the reflow temperature has to be high enough, so that the surface tension can overcome viscosity and smoothen the surface. On the other hand, the temperature cannot be too high, so that the sample does not deform and lose its original symmetry due to gravity. Fused quartz wineglass resonators were reflowed for 30 min at different temperatures, ranging from 1100 °C to 1400 °C, with 1300 °C turned out to be the highest temperature at which no obvious deformation was observed. Therefore, the reflow temperature was set to be 1300 °C for all experiments.

The change of surface roughness over time was studied. The thermal reflow at 1300 °C was applied to blank fused quartz samples with the same surface roughness for different time durations. The results are shown in Fig. 8. Each sample was measured at three different points and the red line represents an average value. The surface roughness was reduced by increasing the time of treatment and the smoothening effect mainly took place in the first 30 min. It can be concluded from Fig. 8 that the reflow time of 1 h was sufficient, reducing the averaged surface roughness from 24.5 nm to 1.9 nm.
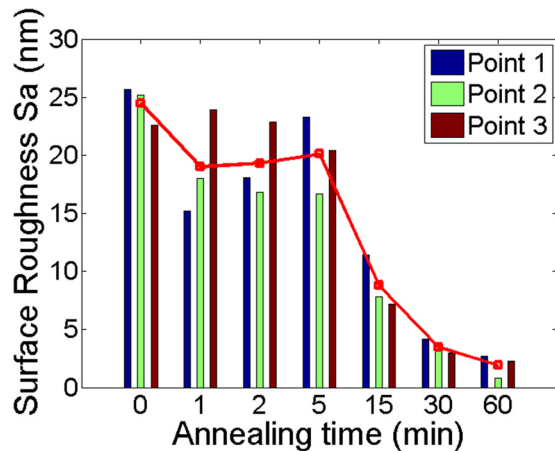
Fig. 8 Surface roughness changes over reflow time
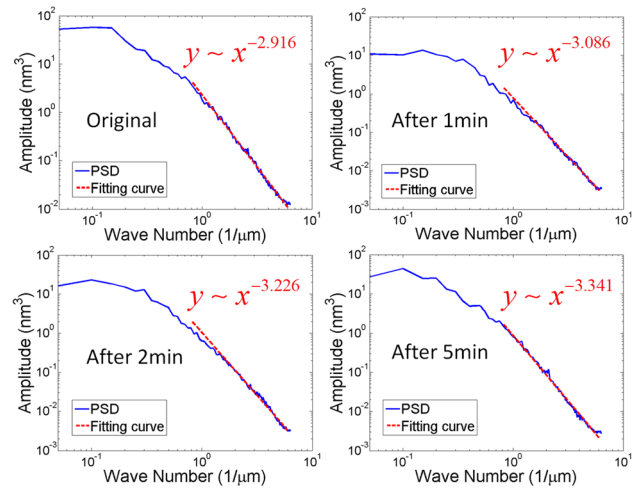
Fig. 9 Power spectral densities of the original surface and surfaces after reflowing for 1 min, 2 min, and 5 min

Figure 8 shows that the averaged surface roughness did not change significantly during the first 5 min, but was greatly reduced with an extended duration of the experiment. To understand the process during the first 5 min, the power spectral density (PSD) was analyzed. PSD of a surface is related to the 2D Fourier transform of the surface height function and it contains more information than an averaged surface roughness. PSD is expressed as

$$P(\mathbf{k}) = \frac{1}{(2\pi)^2} \left| \int_\Omega f(\mathbf{x}) e^{-i\mathbf{k} \cdot \mathbf{x}} d\mathbf{x} \right|^2 \qquad (7)$$

where **k** is the wave number, **x** is the position vector, and $f(x)$ is the height function of the surface. Figure 9 shows the PSD of original surface and surfaces after reflowing for 1 min, 2 min, and 5 min. It shows that these surfaces can be modeled as self-affined [28] and surface roughness exponent α can be extracted to characterize the surfaces. The roughness exponent characterizes the short-range roughness of a self-affined surface and it ranges from 0 to 1. A small value of α implies a rougher local surface, Fig. 10 [28]. For self-affined surfaces, the PSD and surface roughness exponent have a relation

$$P(k) \propto k^{-2-2\alpha}, \quad \text{for } k \gg \xi^{-1} \qquad (8)$$

where ξ is the lateral correlation length of the surface. Figure 9 shows that the surface roughness exponent increases from 0.458 to 0.671, indicating that the short-range roughness is improved by reflow, although the general averaged surface roughness does not change.

Histograms of the original surface and surfaces after reflowing for 5 min, 15 min, and 60 min are shown in Fig. 11, which is a
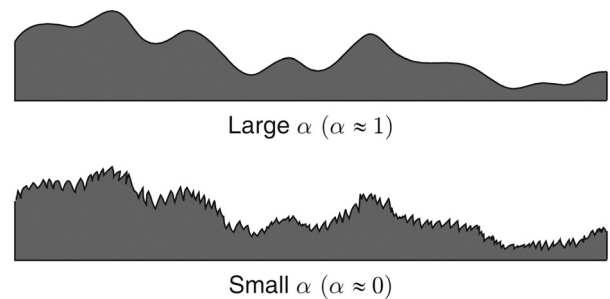
Fig. 10 A comparison of the local surface morphology for similar surfaces with different values of roughness exponent α
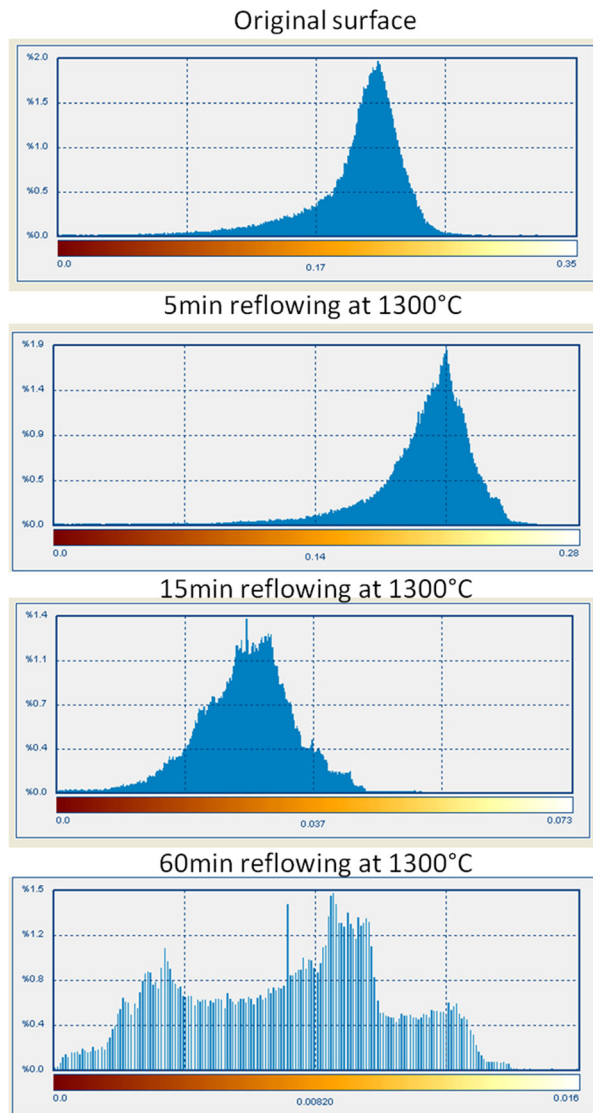
Fig. 11 Histograms of the original surface and surfaces after reflowing for 5 min, 15 min, and 60 min, showing an improvement of long-term surface roughness

characterization of the long-term surface morphology. The X-axis is the height and the Y-axis is the percentage of the area at a corresponding height. The shape and position of the distribution peak in histogram do not change in the first 5 min and only very high elevation regions of the surface are affected. This confirms that only improvement of the short-range roughness happens during this time period. After the first 5 min, the peak becomes more pronounced and shifts to the left, indicating a better surface quality.

4.3 Experiments on Curved Samples. All the previous results are reported for blank fused quartz samples. To show that the same effects can be observed on 3D wineglass structures, the surfaces were measured before and after the thermal reflow. Two glassblown samples from the same batch were tested before and after the 1 h reflow at 1300 °C. The devices were diced into smaller pieces to make sure no other parts of the sample except for the point being measured would be in contact with the AFM tip. The results are shown in Fig. 12. The averaged surface roughness was reduced from 1.9 nm to 0.19 nm. The same smoothening effect was observed in the 3D structures, implying that all the conclusions above are applicable to curved surfaces. Besides, the
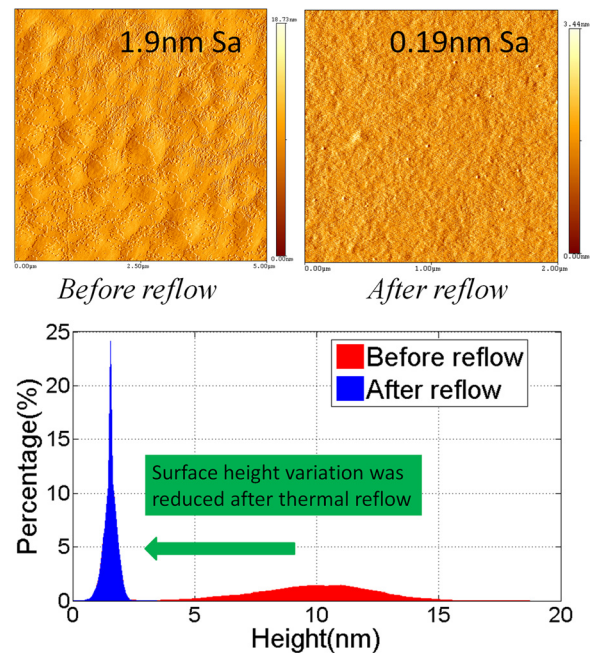
Fig. 12 AFM images of the surface of 3D fused quartz structures and histograms before and after reflow

surface height distribution is lower and more concentrated, indicating a better surface quality after the thermal reflow.

5 Surface Roughness and Quality Factor

One of the goals of this study is to further improve the quality factor of fused quartz wineglass resonators. In this section, the quality factors of resonators with different surface roughnesses were measured, showing a direct correlation between improvement in the quality factor and an improved surface quality.

The experimental procedure for measurement of the quality factor of wineglass resonators is exactly the same as the measurement of resonant frequency, as discussed in Sec. 2. All devices were cleaned by solvent and RCA-1 solution. Next, the devices were placed in dehydration furnace for 45 min to remove all absorbates on the surface before characterization.

Three fused quartz wineglass resonators were tested in this study. First, the resonators were characterized and the quality factors were measured. Then, 10 min of KOH etching was applied to the resonators to roughen the surface and the quality factors were measured again. Then, the resonators were thermally reflowed at 1300 °C for 1 h to improve the surface roughness and the quality factors were measured for the third time. The results of this experiment are shown in Table 3. A direct correlation between the quality factor of resonators and surface roughness can be derived. The reduction of quality factor related to KOH etching was 17,000 on average and the increase of quality factor due to thermal reflow was about 6000. It indicates that a part of the roughening effects due to KOH etching can be compensated by thermal reflow. All other loss mechanisms were remained the same,

Table 3 Quality factors of fused quartz resonators after treatments

Sample number	Quality factor		
	Original	After KOH	After reflow
1	49.9 k	25.6 k	30.2 k
2	60.1 k	42.5 k	46.3 k
3	16.1 k	6.3 k	15.8 k

leading to the conclusion that changes in quality factor were due to surface losses. Quality factors of devices with higher original quality factors were not completely restored probably due to imperfections created during the reflow process, such as the deformation and handling of the devices during the reflow.

6 Conclusion

An analytical model on the effect of imperfections due to release and wet etching of glassblown micro-wineglass fused quartz resonators was developed and supported by experimental results. The predictive frequency of the $n = 2$ wineglass mode shape was within 10% of the finite element results and 20% of the experimental results for thin shells, demonstrating fidelity of the predictive model. The postprocessing methods were analyzed for improvement of the surface quality of fused quartz, concluding that the thermal reflow achieves the best result, reducing the surface roughness from 24.5 nm to 1.9 nm. The direct correlation between a better surface quality and a higher quality factor of the device has been established.

Nomenclature

A = amplitude of the mode
$f(x)$ = height function of the surface
h = thickness of the hemitoroidal shell
k = wave number of the surface
K_0, U_0 = kinetic energy and strain energy of the shell
L = Lagrangian of the shell system
n = mode number
P = power spectral density of the surface
r, θ, φ = radial distance, polar angle, and azimuth angle in spherical co-ordinates
R = radius of the hemitoroidal shell
r_φ = linear displacement along the φ direction
U, V, W = mode shape functions for $\delta r, \delta \theta,$ and $\delta \varphi$
α = surface roughness exponent
β = angular lapping error
$\delta r, \delta \theta, \delta \varphi$ = displacement components of the middle surface of the shell along $r, \theta,$ and φ direction
ξ = lateral correlation length of the surface
ω = angular frequency of the shell

References

[1] Loper, E. J., and Lynch, D. D., 1990, "Vibratory Rotation Sensor," General Motors Corp., Detroit, MI, U.S. Patent No. 4951508 A.
[2] Trusov, A. A., Prikhodko, I. P., Zotov, S. A., and Shkel, A. M., 2011, "Low-Dissipation Silicon Tuning Fork Gyroscopes for Rate and Whole Angle Measurements," IEEE Sens. J., 11(11), pp. 2763–2770.
[3] Cho, J., Gregory, J. A., and Najafi, K., 2011, "Single-Crystal-Silicon Vibratory Cylinderical Rate Integrating Gyroscope (CING)," 16th IEEE International Solid-State Sensors, Actuators and Microsystems Conference (TRANS-DUCERS), Beijing, China, June 5–9, pp. 2813–2816.
[4] Weinberg, M., Candler, R., Chandorkar, S., Varsanik, J., Kenny, T., and Duwel, A., 2009, "Energy Loss in MEMS Resonators and the Impact on Inertial and RF Devices," 15th IEEE International Solid-State Sensors, Actuators and Microsystems Conference (SENSOR), Denver, CO, June 21–25, pp. 688–695.
[5] Loper, E. J., Lynch, D. D., and Stevenson, K. M., 1986, "Projected Performance of Smaller Hemispherical Resonator Gyros," Position Location and Navigation Symposium (PLANS'86), Las Vegas, NV, Nov. 4–7, Vol. 1, pp. 61–64.
[6] Broad Agency Announcement, "Micro Rate Integrating Gyroscope (MRIG)," DARPA/MTO, Announcement No. DARPA-BAA-10-39.
[7] Rozelle, D. M., 2009, "The Hemispherical Resonator Gyro: From Wineglass to the Planets," 19th AAS/AIAA Space Flight Mechanics Meeting, Savannah, GA, Feb. 8–12, pp. 1157–1178.
[8] Xie, Y., Hsieh, H. C., Pai, P., Kim, H., Tabib-Azar, M., and Mastrangelo, C. H., 2012, "Precision Curved Micro Hemispherical Resonator Shells Fabricated by Poached-Egg Micro-Molding," IEEE Sensors Conference, Taipei, Taiwan, Oct. 28–31, pp. 279–282.
[9] Shao, P., Mayberry, C. L., Gao, X., Tavassoli, V., and Ayazi, F., 2014, "A Polysilicon Microhemispherical Resonating Gyroscope," IEEE J. Microelectromech. Syst., 23(4), pp. 762–764.
[10] Bernstein, J. J., Bancu, M. G., Bauer, J. M., Cook, E. H., Kumar, P., Newton, E., Nyinjee, T., Perlin, G. E., Ricker, J. A., Teynor, W. A., and Weinberg, M. S., 2015, "High Q Diamond Hemispherical Resonators: Fabrication and Energy Loss Mechanisms," J. Micromech. Microeng., 25(8), p. 085006.
[11] Eklund, E. J., and Shkel, A. M., 2007, "Glass Blowing on a Wafer Level," IEEE J. Microelectromech. Syst., 16(2), pp. 232–239.
[12] Prikhodko, I. P., Zotov, S. A., Trusov, A. A., and Shkel, A. M., 2011, "Microscale Glass-Blown Three-Dimensional Spherical Shell Resonators," IEEE J. Microelectromech. Syst., 20(3), pp. 691–701.
[13] Cho, J., Nagourney, T., Darvishian, A., Shiari, B., Woo, J., and Najafi, K., 2014, "Fused Silica Micro Birdbath Shell Resonators With 1.2 Million Q and 43 Second Decay Time Constant," Solid-State Sensors Actuators, and Microsystems Workshop (Hilton Head), Hilton Head Island, SC, June 8–12, pp. 103–104.
[14] Schroers, J., Pham, Q., and Desai, A., 2007, "Thermoplastic Forming of Bulk Metallic Glass—A Technology for MEMS and Microstructure Fabrication," IEEE J. Microelectromech. Syst., 16(2), pp. 240–247.
[15] Michael, M., Bordeenithikasem, P., Kim, D., Selden, N., Desai, A., M'Closky, R., and Schroers, J., 2015, "Metallic Glass Hemispherical Shell Resonators," IEEE J. Microelectromech. Syst., 24(1), pp. 19–28.
[16] Cho, J., Yan, J., Gregory, J. A., Eberhart, H. W., Peterson, R. L., and Najafi, K., 2013, "3-Dimensional Blow Torch-Molding of Fused Silica Microstructures," IEEE J. Microelectromech. Syst., 22(6), pp. 1276–1284.
[17] Senkal, D., Ahamed, M. J., Trusov, A. A., and Shkel, A. M., 2013, "High Temperature Micro-Glassblowing Process Demonstrated on Fused Quartz and ULE TSG," Sens. Actuators A, 201, pp. 525–531.
[18] Senkal, D., Ahamed, M. J., Trusov, A. A., and Shkel, A. M., 2014, "Achieving Sub-Hz Frequency Symmetry in Micro-Glassblown Wineglass Resonators," IEEE J. Microelectromech. Syst., 23(1), pp. 30–38.
[19] Senkal, D., Ahamed, M. J., Ardakani, M. H. A., Askari, S., and Shkel, A. M., 2015, "Demonstration of 1 Million-Factor on Microglassblown Wineglass Resonators With Out-of-Plane Electrostatic Transduction," IEEE J. Microelectromech. Syst., 24(1), pp. 29–37.
[20] Wang, Y., and Shkel, A. M., 2016, "Study on Surface Roughness Improvement of Fused Quartz After Thermal and Chemical Post-Processing," IEEE International Symposium on Inertial Sensors and Systems (ISISS), Laguna Beach, CA, Feb. 22–25, pp. 101–104.
[21] Wang, Y., Asadian, M. H., and Shkel, A. M., 2016, "Predictive Analytical Model of Fundamental Frequency and Imperfections in Glassblown Fused Quartz Hemi-Toroidal 3D Micro Shells," IEEE Sensors Conference, Orlando, FL, Oct. 30–Nov. 3, pp. 7–9.
[22] Iliescu, C., Jing, J., Tay, F. E., Miao, J., and Sun, T., 2005, "Characterization of Masking Layers for Deep Wet Etching of Glass in an Improved HF/HCl Solution," Surf. Coat. Technol., 198(1), pp. 314–318.
[23] Choi, S. Y., and Kim, J. H., 2011, "Natural Frequency Split Estimation for Inextensional Vibration of Imperfect Hemispherical Shell," J. Sound Vib., 330(9), pp. 2094–2106.
[24] Rayleigh, J. W. S. B., 1896, The Theory of Sound, Vol. 2, Macmillan, New York, Chap. 10.
[25] Bellomo, N., Lods, B., Revelli, R., and Ridolfi, L., 1980, Generalized Collocation Methods: Solutions to Nonlinear Problems, Springer Science & Business Media, New York, Chap. 2.
[26] Soedel, W., 2004, Vibrations of Shells and Plates, 3rd ed., CRC Press, Boca Raton, FL, Chap. 2.
[27] Kaigawa, H., Yamamoto, K., and Shigematsu, Y., 1994, "Etching of Thermally Grown SiO2 by NH4OH in Mixture of NH4OH and H2O2 Cleaning Solution," Jpn. J. Appl. Phys., 33(7), pp. 4080–4085.
[28] Pelliccione, M., and Lu, T. M., 2008, Evolution of Thin-Film Morphology: Modeling and Simulations, Springer Science & Business Media, New York, Chap. 3.